

Supporting Information for

Accelerated redox conversion of advanced Zn//Fe-Co₃O₄ battery by heteroatom doping

Jiazhuo Li^a, Siwen Zhang^a, Yaxi Ding^a, Ying Sun^a, Jinzhang Yang^a, Hui Li^{a,b}, Tianyi Ma^{b*},
Bosi Yin^{a*}

Experimental section

Preparation of nickel foam

The nickel foam (3 cm × 3 cm in a rectangular shape) was soaked in 6 M HCl solution for 60 mins to remove the oxide layer. Then it was ultrasonically cleaned with deionized water and ethanol to remove the impurities.

Preparation of Co₃O₄ electrode material

1.5 g Co(NO₃)₂·6H₂O and 1.5 g C₆H₁₂N₄ were dissolved in 30 mL deionized water under stirring. The mixture was further homogenized for 1 hour. The resulting pink solution was transferred to a Teflon-lined stainless steel autoclave (80% filling ratio). The pre-treated nickel foam was immersed into the solution, and the autoclave was sealed. After the hydrothermal treatment at 120 °C for 16 h, the reactor was completely cooled to room temperature. The nickel foam was washed repeatedly with deionized water and absolute ethanol to remove the free nanoparticles and residual reactants. Then, the nickel foam was dried in a vacuum oven at 60 °C for 12 h and calcined in a muffle furnace at 450 °C in the air for 2 h to obtain the Co₃O₄ electrode material grown on the Ni foam.

Preparation of Fe-Co₃O₄ electrode material

$\text{Fe}(\text{NO}_3)_3 \cdot 9\text{H}_2\text{O}$ was added to the solution containing $\text{Co}(\text{NO}_3)_2 \cdot 6\text{H}_2\text{O}$ (Fe/Co ratios of 0.2, 0.4, 0.5, 0.7: 1) and $\text{C}_6\text{H}_{12}\text{N}_4$. The synthesis followed the same steps as described in the previous section.

Characterizations

The crystal structure was investigated by powder X-ray diffraction (XRD) (Bruker D8-Advance) with $\text{CuK}\alpha$ radiation ($\lambda = 0.15406$ nm). The surface morphology was studied with a field emission scanning electron microscope (SEM, HITACHI, SU8010). The microstructure was characterized by an ultra-high-resolution transmission electron microscope (TEM, JEM-2100). The X-ray photoelectron spectra (XPS) were obtained on an XPS spectrometer (ESCALAB 250 Xi, Thermo Scientific Escalab). The data were calibrated by referencing C1s peak to 284.6 eV.

The Co: Fe ratio was determined by inductively coupled plasma mass spectrometer (ICP-MS, Agilent ICP-OES 725 ES). The surface area and pore size distribution were investigated by the Brunauer-Emmett-Teller method (BET, QuantaAutosorb IQ). Fourier transform infrared spectroscopy (FTIR) was investigated by German Bruker Tensor II, and the test wavelength ranged from 500 cm^{-1} to 4000 cm^{-1} . The mass loading of the active materials was measured using the weight difference of the electrode before and after the hydrothermal reaction of the active material, using an analytical balance (BT 25 S, Sartorius, sensitivity: 0.01 mg). The mass loading of the Fe- Co_3O_4 on Ni foam was 1.10 mg/cm^2 .

Electrochemical Characterization

The electrochemical properties of the electrodes, including cyclic voltammetry (CV), galvanostatic cycling with potential limitation (GCPL), and electrochemical impedance

spectroscopy (EIS), were conducted using a multichannel electrochemical analyzer (VMP3, Bio-Logic-Science Instruments) and CHI electrochemical workstation (760 E, Chenhua). The electrochemical performance was tested in a three-electrode configuration filled with 3 M KOH aqueous solution, with $\text{Co}_3\text{O}_4@\text{Ni}$ or $\text{Fe-Co}_3\text{O}_4@\text{Ni}$ (1 cm × 1 cm) as the working electrode, respectively, with Hg/HgO and platinum sheet as the reference and counter electrode. The energy density (E , Wh/kg) and power density (P , W/kg) of the devices were calculated using the following formula ¹:

$$C_{SP} = \frac{It}{m\Delta U} \quad (1)$$

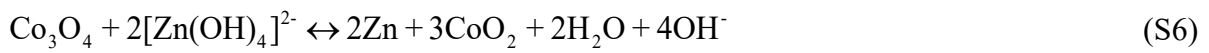
$$E = \frac{1}{2}C_{SP}U^2 \quad (2)$$

$$P = \frac{E}{t} \quad (3)$$

- C_{SP} is the specific capacitance (F/g),
- I is the constant discharge current (A),
- t is the discharge time (s),
- m is the mass loading (g),
- U is the operating voltage.

The electrochemical performance of the battery was tested in a 3 M KOH aqueous solution, with the $\text{Co}_3\text{O}_4@\text{Ni}$ or $\text{Fe-Co}_3\text{O}_4@\text{Ni}$ as the cathode and Zn as the anode. The device was tested in a two-electrode configuration. All experiments were carried out at room temperature.

Equation ^{2,3} :



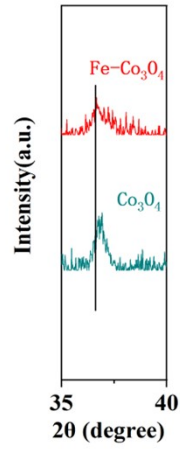


Fig. S1. Part of the XRD patterns of Co_3O_4 and $\text{Fe-Co}_3\text{O}_4$.

Table S1. Element contents of Fe-Co₃O₄ measured by ICP-MS.

Materials	Co (wt%)	Fe (wt%)
Fe-Co₃O₄	8.980	0.584

Note: The results show that the Co content is 8.980, and that of Fe is 0.584.

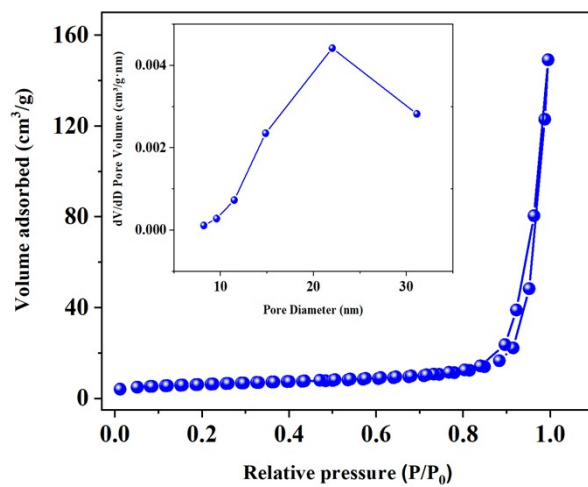


Fig. S2. N_2 adsorption-desorption isotherms and pore size distribution of Co_3O_4 .

Fig. S3. SEM images of (a,b) Co_3O_4 , TEM images of (c,d) Co_3O_4 .

Fig. S4. (a-c) EDS elemental mapping images of $\text{Fe-Co}_3\text{O}_4$, (d) EDS spectrum of $\text{Fe-Co}_3\text{O}_4$.

Fig. S5. (a-c) CV curves of the Fe-Co₃O₄ (Co: Fe=1: 0.2, 0.5, 0.7) electrodes at different scan rates, (d-f) GCPL curves of the Fe-Co₃O₄ (Co: Fe=1: 0.2, 0.5, 0.7) electrodes at various current densities.

Fig. S6. (a) CV curves of the Fe-Co₃O₄ electrode at different scan rates, (b) CV curves of the Co₃O₄ electrode at different scan rates, (c) GCPL curves of the Co₃O₄ electrode at various current densities, (d) GCPL curves of the Fe-Co₃O₄ electrode at various current densities.

Note: The CV curves were measured at the different scan rates (1, 2, 3, 5, 8, 10 mV/s) and in the voltage scan window of 0.0-0.4 V (Fig. S6a-b). The integrated area of the Fe-Co₃O₄ CV curves is significantly larger than that of Co₃O₄. This indicates that Fe doping greatly improves the specific capacity of the material. Fig. S6c-d shows the GCPL curves of Co₃O₄ and Fe-Co₃O₄ at different current densities. It can be seen that there are two pairs of redox peaks, one is for the transformation of Co₃O₄ to CoOOH, and the other is attributed to the CoOOH conversion to CoO₂. The reactions were the following ⁴:



As shown in the Fig. S6b, the conversion of Co²⁺ to Co³⁺ and Co³⁺ to Co⁴⁺ corresponding to

the two oxidation peaks respectively can be seen. Reduction peaks are just the opposite. The shape of the measured curve is different from rectangular-shaped CV curves of typical double-layer electrode material, which explained the pseudocapacitance behavior of Co_3O_4 ⁵. The mirror symmetry and the stability of the CV curves are perfect, indicating that the material has high redox reversibility.

Fig. S6c-d show the GCPL curves of Co_3O_4 and $\text{Fe-Co}_3\text{O}_4$ at different current densities (2, 3, 4, 6, 8, and 10 A/g). The charge-discharge platform of GCPL curves is consistent with the redox platform height of the CV curves measured before.

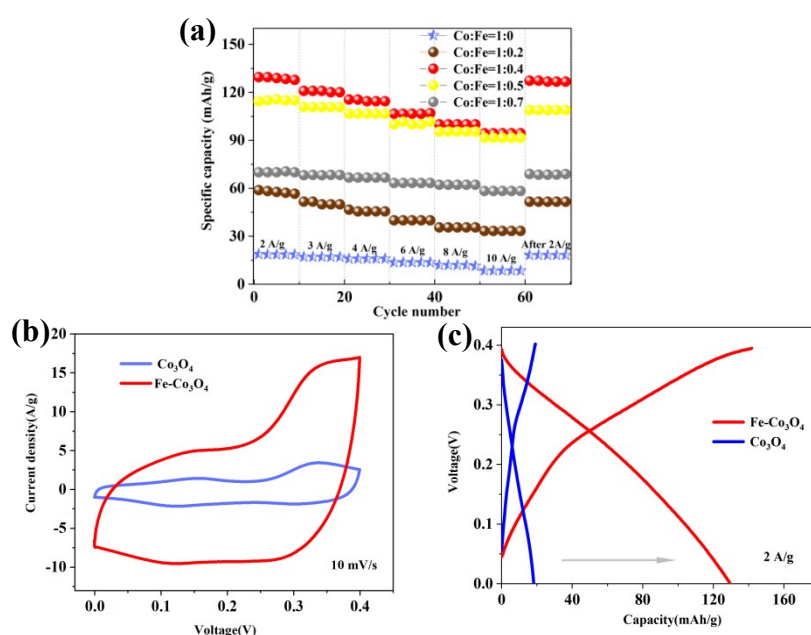


Fig. S7. (a) The rate performances of the electrode materials with different Co: Fe ratios, (b) Comparison of CV curves of Co_3O_4 and $\text{Fe-Co}_3\text{O}_4$ electrodes at 10 mV/s, (c) Comparison of GCPL curves of Co_3O_4 and $\text{Fe-Co}_3\text{O}_4$ electrodes at 2 A/g.

Note: The rate performance of the electrode materials is shown in Fig. S7a. The results pointed out that the best electrochemical performance was achieved when the Co: Fe was 1:0.4. By comparing the curves (Fig. S7b-c), the capacity of the material was significantly improved after Fe doping at 2 A/g (from 17.99 to 128.97 mAh/g). The introduction of Fe ions leads to the reduction of grain size and an increase in defects. The generation of oxygen defects and the increase of specific surface area will enlarge the number of active sites of the material itself and increase the reaction intensity with OH^- , thus greatly accelerating the redox conversion inside the battery, which improves the electrochemical performance of the battery⁶.

Fig. S8. (a) Relationship of Co_3O_4 between $\log(i)$ and $\log(v)$, (b) Capacitive contribution of Co_3O_4 at 10 mV/s, (c) Capacitive contributions of Co_3O_4 at different scan rates, (d) Relationship of $\text{Fe-Co}_3\text{O}_4$ between $\log(i)$ and $\log(v)$, (e) Capacitive contribution of $\text{Fe-Co}_3\text{O}_4$ at 10 mV/s, (f) Capacitive contributions of $\text{Fe-Co}_3\text{O}_4$ at different scan rates.

Note: Since Co_3O_4 has a very typical spinel structure, redox reactions occur on the surface and in bulk. Therefore, the storage behavior of Co_3O_4 is between a battery and a capacitor ⁷. The contribution of pseudocapacitance is usually calculated by the following formula ^{8,9}:

$$i = av^b \quad (6)$$

$$\log(i) = \log(a) + b\log(v) \quad (7)$$

v (mV/s) is the scanning rate, and i (mA) is the corresponding peak. a and b are the adjustment parameters in the equation, where b is calculated by linear curve fitting so that the kinetic information related to the electrode in the electrochemical reaction can be calculated. When the b value at different potentials is equal to 0.5 or 1, which indicates that the investigated compound is a battery-type or capacitor-type material ¹¹. While $0.5 < b < 1$, pseudocapacitance and capacitive are controlled simultaneously, meaning that the material is transitioning between capacitive and battery-type materials. In general, b increases with the increase of the surface capacitance contribution, that is, the decrease of the influence of the pseudocapacitance control process.

The fitting process of b is shown in Fig. S8a and 8d. The b values for the four peaks were 0.85626, 0.90054, 0.91852, and 0.85268, respectively, indicating that the electrochemical reaction of the material is controlled by pseudocapacitance and capacitive. However, the b value is closer to 1, and the kinetics are faster, so the capacitance plays a dominant role. By comparing the b value of Co_3O_4 and Fe- Co_3O_4 (Fig. S8a and S8d), it was found that it decreases after Fe doping, indicating that doping makes the material more inclined to behave as a battery-type material. This greatly improves the electrochemical performance of the Zn-Co battery.

To explore where the pseudocapacitance contribution occurs, the following equation was applied ¹⁰:

$$i = k_1v + k_2v^{1/2} \quad (8)$$

Where k_1v and $k_2v^{1/2}$ represent the capacitive control and pseudocapacitance control of the current, respectively, and it can be transformed into:

$$i/v^{1/2} = k_1v^{1/2} + k_2 \quad (9)$$

The k_1 value is obtained following linear fitting. As shown in Fig. S8b and 8e, the capacitance contribution of Co_3O_4 and Fe- Co_3O_4 at a scan rate of 10 mV/s is 94.07% and 74.50%. Comparing the capacitive contribution of the two materials at different scanning rates (Fig. S8c and 8f,) points out that Fe doping will significantly reduce the contribution of the capacitive, leading to better electrochemical performance ¹¹.

Fig. S9. (a) CV curves of the Zn//Co₃O₄ battery at various scan rates, (b) GCPL curves of the Zn//Co₃O₄ battery at different current densities, (c) The EIS curves of Zn//Co₃O₄, Zn//Fe-Co₃O₄ and after 9000 cycles-Zn//Fe-Co₃O₄ batteries.

Note: After 9000 cycles, the EIS curve of Zn//Fe-Co₃O₄ is also plotted in the frequency range of 100 kHz to 0.01 Hz at an open circuit potential with an AC perturbation of 5 mV. The graph shows the curve forming a semi-arc in the high-frequency region and an inclined straight line with a radian of about 45° in the low-frequency region. The interfacial properties of the electrode and the corresponding charge transfer resistance are located in the high-frequency region. The straight line in the low-frequency region is due to the diffusion resistance and the electrolyte diffusion inside the electrode pores ⁵.

References

- 1 G. Li, M. Chen, Y. Ouyang, D. Yao, L. Lu, L. Wang, X. Xia, W. Lei, S. Chen, D. Mandler, Q. Hao, *Appl. Surf. Sci.*, 2019, **469**, 941–950.
- 2 J. Li, Y. Ding, S. Zhang, H. Li, B. Yin, T. Ma, *J. Power Sources*, 2022, **524**, 231074.
- 3 W. Shang, W. Yu, Y. Liu, R. Li, Y. Dai, C. Cheng, P. Tan, M. Ni, *Energy Stor. Mater.*, 2020, **31**, 44–57.
- 4 Y. Zhang, L. Li, S. Shi, Q. Xiong, X. Zhao, X. Wang, C. Gu, J. Tu, *J. Power Sources*, 2014, **256**, 200–205.
- 5 D. Kong, J. Luo, Y. Wang, W. Ren, T. Yu, Y. Luo, Y. Yang, C. Cheng, *Adv. Funct. Mater.*, 2014, **24**, 3815–3826.
- 6 Y. Xu, Q. Ding, L. Li, Z. Xie, G. Jiang, *New J. Chem.*, 2018, **42**, 20069–20073.
- 7 K. Owusu, L. Qu, J. Li, Z. Wang, K. Zhao, C. Yang, K. Hercule, C. Lin, C. Shi, Q. Wei, L. Zhou, L. Mai, *Nat. Commun.*, 2017, **8**, 14264.
- 8 V. Augustyn, P. Simon, B. Dunn, *Energy Environ Sci.*, 2014, **7**, 1597–1614.
- 9 V. Augustyn, J. Come, M. Lowe, J. Kim, P. Taberna, S. Tolbert, H. Abruña, P. Simon, B. Dunn, *Nat. Mater.*, 2013, **12**, 518–522.
- 10 J. Wang, J. Polleux, J. Lim, B. Dunn, *J. Phys. Chem. C*, 2007, **111**, 14925–14931.
- 11 T. Brezesinski, J. Wang, S. Tolbert, B. Dunn, *Nat. Mater.*, 2010, **9**, 146–151.